university of groningen

faculty of science and engineering

Setting Sights on a New Target:

Working Towards Understanding Transitional Flow from a Capillary

Marco Vogt
S3295575

university of groningen

faculty of science and engineering

University of Groningen

Setting Sights on a New Target: Working Towards Understanding Transitional Flow from a Capillary

Bachelor Research Project

To fulfill the requirements for the degree of
Bachelor of Science in Applied Physics
at the University of Groningen under the supervision of
first examiner Prof. Dr. ir. R. Hoekstra,
second examiner Dr. T. Schlathölter,
and daily supervisor K. I. Bijlsma, MSc

Marco Vogt
S3295575

July 9, 2021

Contents

Acknowledgments

To begin, I would like to express my sincerest thanks to Professor Hoekstra for his approachability, guidance, and welcoming attitude. In a similar vein, I also thank my daily supervisor Klaas Bijlsma for his help and willingness to teach me in the lab. Them, along with Subam, Mart, and the rest of the QISD research group not only treated me with kindness and respect, but helped me find my passion for physics once again.

Thank you also to Dr. Thomas Schlathölter for agreeing to be my second examiner, and lastly I would like thank my parents Heike and Gunnar Vogt for their continued support throughout my studies.

Abstract

In this crossed beam experiment, a narrow beam of selected ions is aimed at a target of H_2 gas. The installation of a movable capillary for the injection of H_2 has created a new set of challenges in determining the optimal capillary position and the shape of the target profile.

On April 26, 2021, the CHEOPS experimental setup in Groningen was fitted with a 100 mm long and 1 mm diameter capillary mounted to a 3-axis translation stage. By manipulating the position of the capillary, the optimal setting for maximum target intensity at the beam was found to be X = 12.65 mm, Z = 11.50 mm. At heights lower than Y = 50.0 mm, the capillary was found to physically block the charge exchange products when used for time of flight spectroscopy. Scanning the capillary along the X and Y direction and recording the countrate at varying positions allows for a visualization of the target profile. This was conducted for hydrogen and deuterium target molecules at flow rates of 2, 7, and 20 percent of 5 ml/min.

1 Introduction

Moore's law says that the number of transistors on a microchip doubles every two years, and since the 1970's this law has held true. High demand for faster and more affordable processors has sustained innovation in the industry of microchip manufacturing, specifically the field of nanolithography. Producing high transistor-density chips becomes an increasingly difficult task, and continually pushes the bounds of physics and industry. The coming generation of microchips are produced using Extreme Ultraviolet (EUV) technology, which utilizes 13.5 nm light to print patterns on a wafer.

ASML's newest line of EUV machines generate 13.5 nm light by turning tin into plasma. By shooting a laser at a tin droplet, a plasma is created that contains tin ions in a wide variety of excited states. When these excited ions relax, they emit radiation, with a peak at 13.5 nm in wavelength [1]. The trouble arises with the mirrors needed to collect and focus this wavelength of light. Heavy tin ions collide with the extremely sensitive mirrors, causing them to lose efficiency quickly.

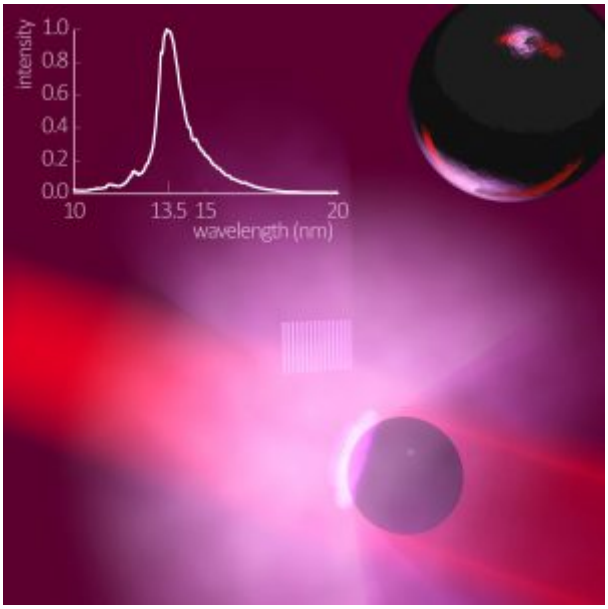

Figure 1.1: Artist's rendering of a laser striking a tin droplet. Image from [1].

This issue may be resolved by using hydrogen gas as a buffer between the tin ions and the mirror. At the ZERNIKELEIF (Zernike Low Energy Ion beam Facility) at the University of Groningen, the interactions between tin and molecular hydrogen are looked at in detail. By aiming a beam of tin ions at a hydrogen gas target and observing the behavior of the collision products, fundamental characteristics can be determined, such as the collision cross section.

On April 26, 2021, the experimental setup in Groningen was upgraded with a new, movable capillary, allowing the hydrogen target to be moved with respect to the beam. This thesis focuses on the calibration of the new capillary and the effects of capillary positions in time-of-flight measurements.

2 Theory

2.1 Molecular Effusion

To begin, it is convenient to define the difference between diffusion and effusion. If two regions of varying gas pressures are separated by a barrier with a hole, the gas is said to *effuse* if the mean free path of the gas (usually denoted by λ) is larger than the diameter of the hole [2]. Conversely, if the molecular mean free path is smaller than the hole diameter, the molecules are said to *diffuse* [2].

The mean free path of a particle can be determined using the formula

$$\lambda = \frac{k_B T}{\sqrt{2}\pi d^2 P} \tag{1}$$

[2]. k_B is the Boltzmann constant, T is the temperature in Kelvin, d is the particle diameter, and finally P is the pressure.

2.2 Flow Regimes

To understand the problem at hand, it is important to understand the impact of flow regimes on capillary effusion. The Knudsen numbers can be defined as

$$K_L = \frac{\lambda}{L} \qquad \text{and} \qquad K_D = \frac{\lambda}{D},$$

where λ is the mean free path of the gas molecules and L and D are the characteristic flow dimensions (the length and diameter of the capillary, respectively, for the purposes of this thesis). The mean free path of the molecules in the gas is large at low pressure.

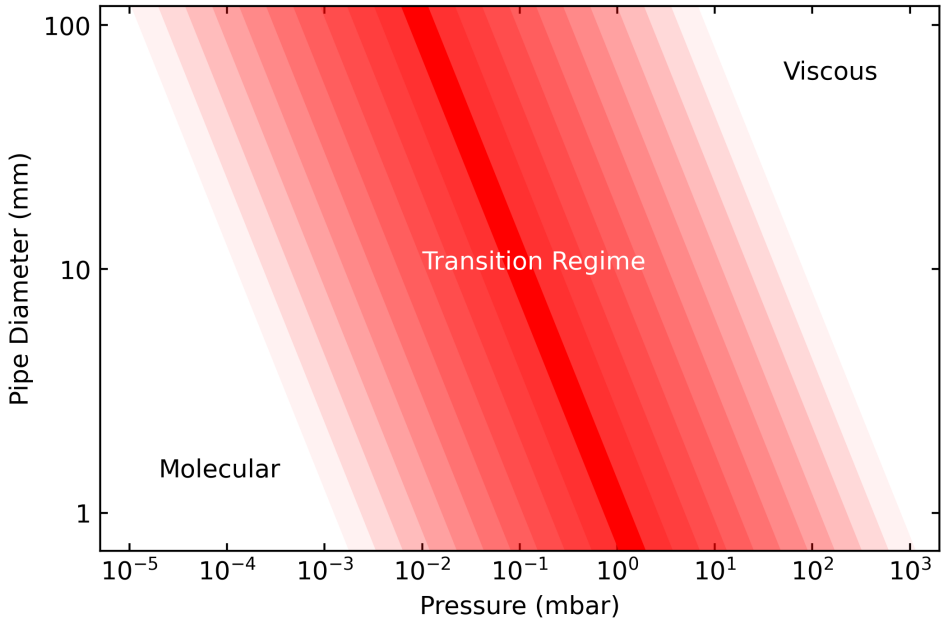

Figure 2.1: Flow regimes described by pressure and pipe diameter. Adapted from [3].

When $K_L > 1$, the setup is considered to be in the molecular flow regime, meaning that the flow is characterised by individual molecules traveling through the flow channel, and that molecule-molecule collisions can be effectively neglected [4]. This is usually the case in high/ultra high vacuum setups [3]. When $K_D < 1$, the flow is typically described as viscous, meaning it is more easily treated as a fluid using the Reynolds number [4][3].

The profiles and flow characteristics of molecular beams are well studied at large K_L, i.e. low driving pressure [5]. However, in beam-beam collision experiments, Knudsen numbers tend to be in the range of $K_L \approx 1$ to $K_D \ll 1$ [4]. If $K_L \leq 1$ and $K_D > 1$ (that is if $D < \lambda \leq L$), the flow is said to be in a transition regime [4], making theoretical descriptions of the flow complex and typically inaccurate with respect to empirical data [5]. Figure 2.1 shows where the transition regime lies with respect to pressure and channel diameter.

2.3 Molecular Flow Through a Cylindrical Channel

Following the derivation of Scoles et al. (see reference [5]), the target intensity, I, can be described as a function of the angle from the center of the capillary, θ. The following equations are only applicable in the so-called 'transparent mode of operation,' or when $K_L \gg 1$ [5]. However, they may serve as a useful starting point in determining the target profile for Knudsen numbers closer to 1. Figure 2.2 shows a schematic of length L and diameter D, and gives a clearer picture of how the angle from the capillary is defined.

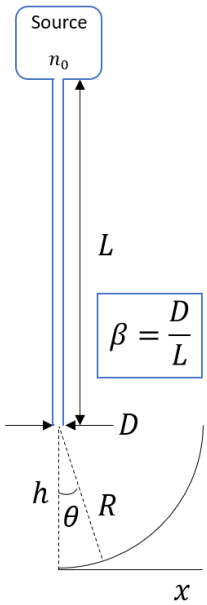

Figure 2.2: Schematic of a capillary, defining the angle from the capillary, θ.

Starting with the intensity:

$$I(\theta) = \frac{v_0}{\pi}\sigma j(\theta) \tag{2}$$

Here, v_0 is the rate at which molecules in the gas reservoir enter a unit area of the orifice. The orifice has a cross-sectional area of σ. The term $j(\theta)$ gives the angular dependence.

$$j(\theta) = \begin{cases} \alpha\cos\theta + \frac{2}{\pi}\cos\theta\left[(1-\alpha)R(q) + \frac{2}{3q}(1-2\alpha)\{1-(1-q^2)^{3/2}\}\right] & \text{if } q \leq 1 \\ \alpha\cos\theta + \frac{4}{3\pi q}(1-2\alpha)\cos\theta & \text{if } q > 1 \end{cases} \tag{3}$$

The value of q is determined by the length and diameter of the capillary, as well as the angle, θ:

$$q = \frac{L}{D}\tan\theta. \tag{4}$$

$R(q)$ is given as

$$R(q) = \arccos q - q\sqrt{(1-q^2)}. \tag{5}$$

The constant α is given as a function of the capillary shape factor, $\beta = D/L$.

$$\alpha = \frac{1}{2} - \frac{1}{3\beta^2}\left(\frac{1-2\beta^3+(2\beta^2-1)(1+\beta^2)^{1/2}}{(1+\beta^2)^{1/2}-\beta^2\sinh^{-1}(\frac{1}{\beta})}\right) \tag{6}$$

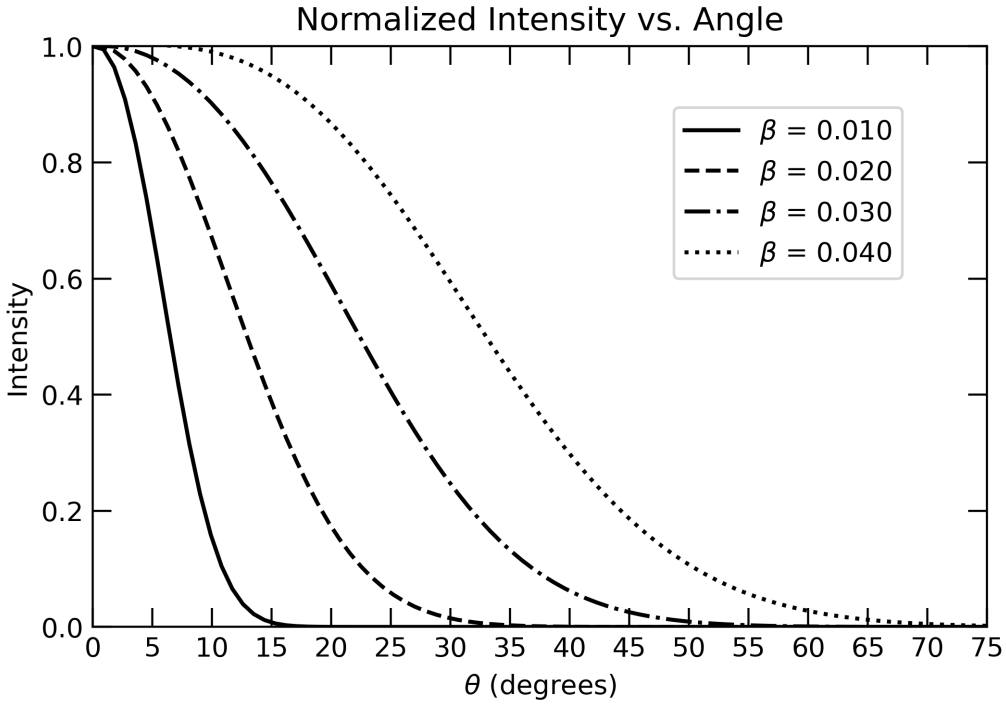

Figure 2.3: Normalized intensity vs angle for varying capillary shape factors, β.

Figure 2.3 shows that the intensity of a capillary of $\beta = 0.01$ drops off dramatically, with a near-zero intensity at $\theta = 15°$. An increase in β increases the width of the angular distribution. Note that the capillary used in this thesis has a shape factor of $\beta = 0.01$.

3 Experimental Setup

The experiments described in this bachelor thesis were conducted at the ZERNIKELEIF facility, at the Zernike Institute for Advanced Materials (ZIAM) at the University of Groningen. The main objective of the set up to be described is to investigate the interactions between tin ions and molecular hydrogen. In particular, this thesis focuses on the effects of the newly installed capillary, mounted to an XYZ translation stage. Figure 3.1 shows a rendering of the experimental setup used by the Quantum Interactions and Structural Dynamics research group in Groningen, which is part of ZIAM.

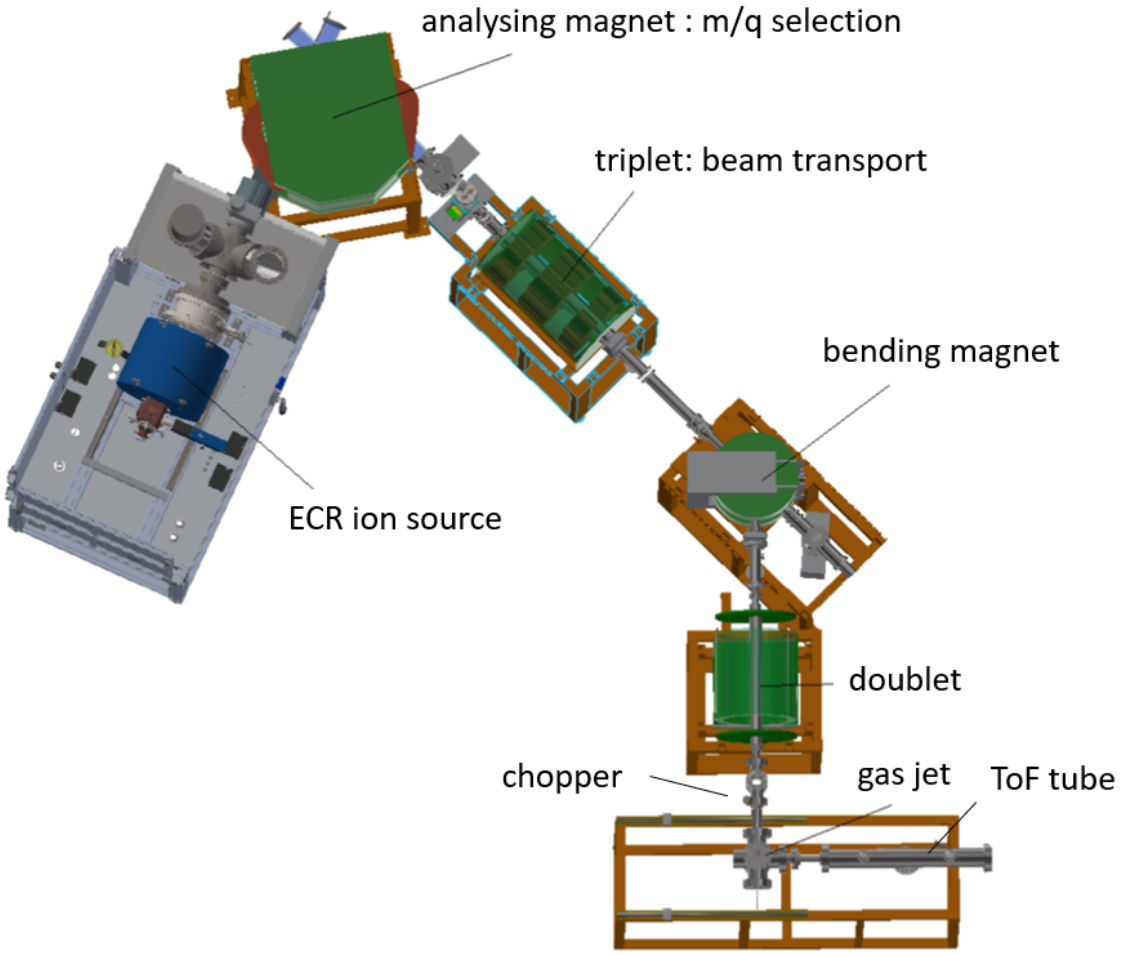

Figure 3.1: Top-down rendering of the experimental setup used at ZERNIKELEIF. Image courtesy of QISD.

3.1 ECRIS

The logical first step in making an ion beam is producing ions. An Electron Cyclotron Resonance Ion Source (ECRIS) is used to create a plasma, from which charged ions can be extracted. The plasma is confined by a magnetic field, created by a hexapole magnet. The electrons in the device are heated by electron cyclotron resonance, powered by 14GHz microwaves from an external radio frequency

power source.

The ions are created by a process called electron impact ionization. In this process, the highly energetic electrons collide with the atoms/molecules of the operator's choosing, and produce ions [6]. The ions get their energy from a high voltage source. Also attached to the ECRIS is a puller lens, which can be negatively biased to pull positively-charged ions towards the 110° analyzing magnet, where the beam begins to form.

3.2 110° Magnet

The selection of the desired ions is done via a 110° analyzing magnet. This magnet selects ions of desired charge state based on the mass-charge ratio of the ion. The magnetic field strength is set to a value in accordance with the following formula:

$$B = 113.6 \cdot \sqrt{\frac{m}{q} \cdot V}$$

where m is the mass of the ion in amu, q its charge state, and V the high voltage on which the source is operated, which defines the energy of the ion (qV) in keV. This magnetic field is then tuned using a fine adjustment knob to ensure maximum transmission of the desired ions.

3.3 Faraday Cup

With a beam of specified ions made, the position and strength of the beam is determined using a Faraday cup. A Faraday cup is a metal container that can be used to detect ions. The opening of the cup faces the incoming ion beam, allowing the charged particles to strike the "collector," or back of the cup. The interaction between ions and the metal causes a charge exchange to take place. The current from cup to ground is then measured, which is used as an indicator of how many particles are striking the cup. Since these interactions take place at Ultra High Vacuum (UHV), it is assumed that all particles interacting with the cup are from the ion beam.

There are two Faraday cups present on the setup used in this thesis. The first sits right after the analyzing magnet, and the second is mounted at the end of the ion beam. The first Faraday cup can be lowered into the beam path, allowing for the operator to adjust the ECRIS and analyzing magnet settings to create the strongest beam possible. The second Faraday cup is positioned such that losses along the beam path can be determined and minimized. This cup also has some added features: a cap and guard ring that can be electrically biased, and a 2-dimensional translation stage. Applying a voltage to either the cap or guard ring suppresses the effects of secondary electron emission, meaning that the measured current will more accurately reflect the number of ions being collected by the cup. The ion beam passes through many focusing and bending magnets, making it very susceptible to small differences in magnet settings. The translation stage allows the Faraday cup to be centered on the ion beam, making more accurate measurements possible.

3.4 Quadrupole Magnets

Along the beam path, there are five quadrupole magnets, set up in a triplet and doublet configuration. After the first Faraday cup is lifted, the ions travel through the triplet, then through a 45° magnet (with a similar operating principle as the 110° magnet), and then through the doublet.

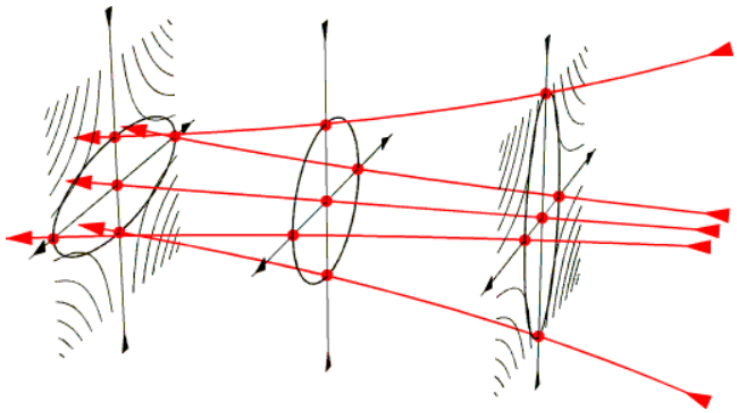

Figure 3.2: Magnetic field lines for constant axial magnetic field, passing though two quadrupole magnets. Image from [7].

Figure 3.2 shows the magnetic field lines between a quadrupole doublet along the path of an ion beam. It can be seen that the magnetic field lines form an elliptical shape as they pass through the magnets. Similarly, the ion beam is focused into an elliptical shape as it passes through each quadrupole. Each quadrupole causes the beam to focus along one axis, and broaden along the perpendicular axis, but the focusing effect is stronger than the broadening effect. By passing through quadrupoles with alternating orientations, the ion beam can be effectively focused by tuning the power delivered to each quadrupole magnet.

3.5 CHEOPS

The main focus of this setup is CHEOPS (CHarge Exchange Observed by Particle Spectroscopy), which houses the components necessary for the following experiments. CHEOPS contains extraction plates necessary for taking time-of-flight measurements (described later), a 'chopper' that pulses the beam, as well as a movable capillary for the injection of a gas target. A cutaway diagram of CHEOPS is visible in Figure 3.3. The capillary has a diameter of 1.016 mm, and a length of 100 mm, giving it a shape factor of $\beta = D/L = 1.016/100 \approx 0.01$. The region above the capillary is connected to a computer-controlled flow controller, that lets in a specific amount of gas (usually H_2), which effuses into the CHEOPS set up, providing a target for the ion beam. The flow controller allows the operator to select a percentage of the maximum allowed flow (5 mL/min). Reductions in current as a result of the charge exchange interactions with the target molecules can be measured by the Faraday cup, also attached to the CHEOPS setup in the direction of the beam.

Also of note is that there is a 1 mm diameter diaphragm at the ion beam's entrance to the collision chamber. This ensures that the beam is narrow and localized, at the cost of beam intensity. For time-of-flight measurements however, it is crucial that the beam intersects the target between the extraction

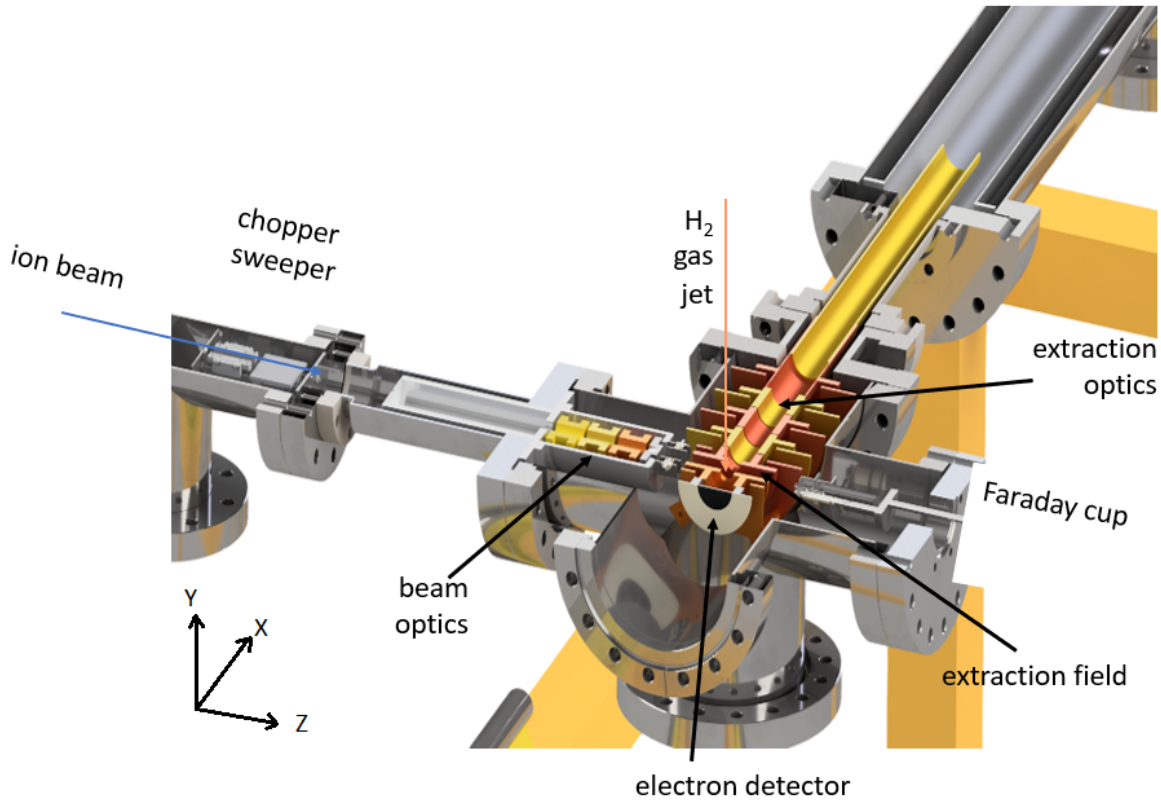

Figure 3.3: Cutaway diagram of CHEOPS. Image courtesy of QISD.

plates, making a narrow and predictably-placed beam necessary.

3.6 XYZ Manipulator

The main focus of this bachelor thesis is the installation of a movable capillary, as opposed to the fixed one that was attached to CHEOPS previously. This allows for the target to be positioned in such a way that the ion beam overlaps with the region of peak target intensity. The coordinate system used for this setup is shown in Figure 3.4. The range of motion of the capillary is limited by the position of the extraction plates in the X-direction, and the size of the capillary flange with respect to the tube that houses it in the Z-direction. For the X-direction, there is 10 mm of space between the extraction plates. To ensure that the capillary did not touch the extraction plates, the capillary was moved until it was just out of electrical contact with either extraction plate. These two positions were set as safe positions to ensure that the capillary would not scratch or be bent by the extraction plates. The range of motion in every direction is as follows:

- X (towards time-of-flight): 8.5 - 16.5 mm $\implies$ 8 mm range
- Y (along the capillary): 40 - 110 mm $\implies$ 70 mm range
- Z (along the path of the beam): 4.5 - 16.5 mm $\implies$ 12 mm range

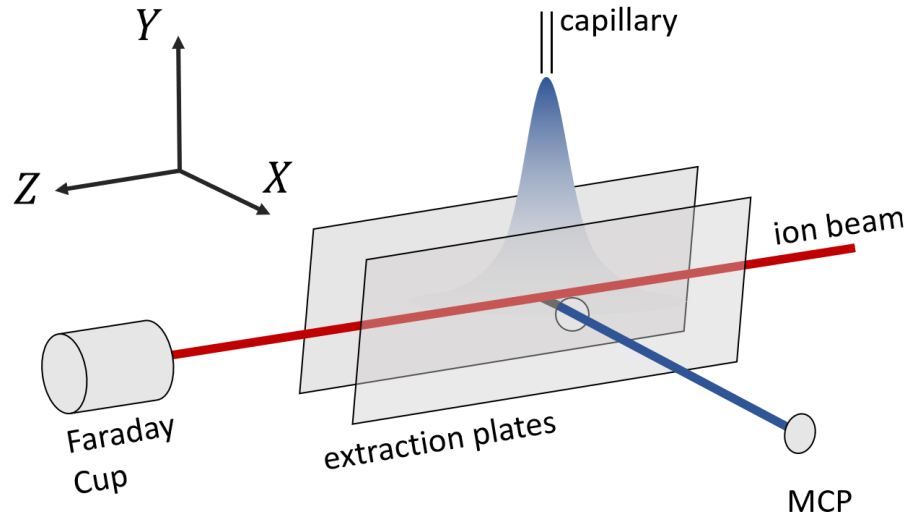

Figure 3.4: Coordinate system used in CHEOPS. Image courtesy of K. Bijlsma, QISD.

3.7 Time-of-Flight

Time-of-flight (TOF) spectroscopy is used to determine the mass and charge state of the charge exchange products. By using a number of electrically biased plates and lenses, the charged particles are pulled through a long tube of known length. Using a microchannel plate (MCP) detector that is sensitive to individual ions, the flight time of the charge exchange products can be recorded. The charge of these particles determine their energy, and combined with mass, the particle's velocity can be determined. Figure 3.5 shows how an H_2^+ molecule may dissociate between the extraction plates. Note that the orientation of the molecule determines the direction of the resulting protons. Typically only H_2 molecules whose axis is in line with the TOF chamber pass through the extraction diaphragm. These protons typically have an initial forward or backward velocity, creating a detectable time difference, ΔT, between them.

In order to measure the time of flight, an initial time, t_0, must be known. For that reason, a chopper system is implemented. The chopper is made up of two charged plates, that can be biased to bend the ion beam before it enters CHEOPS. By alternating the plate potentials periodically, the beam bends up and down over the diaphragm. This means that the ion beam only passes through the diaphragm for short burst of time, in the order of nanoseconds. Once the flight times of the particles are recorded, they can be combined into a histogram showing distinct peaks from the charge exchange products.

A typical time-of-flight spectrum shows four distinct peaks. In order of time the particle travels, these peaks correspond to forward emitted protons (H_f^+), zero-energy protons (H_z^+), backward emitted protons (H_b^+), and ionized molecular hydrogen (H_2^+). Due to the diaphragm limiting the transmission of the particles, the forward emitted proton peaks are typically larger than the backward emitted proton peaks. This is because the backward emitted protons travel for a longer time, causing more of them to 'miss' the diaphragm. Figure 3.6 shows what a typical time-of-flight spectrum looks like for an H_2 target.

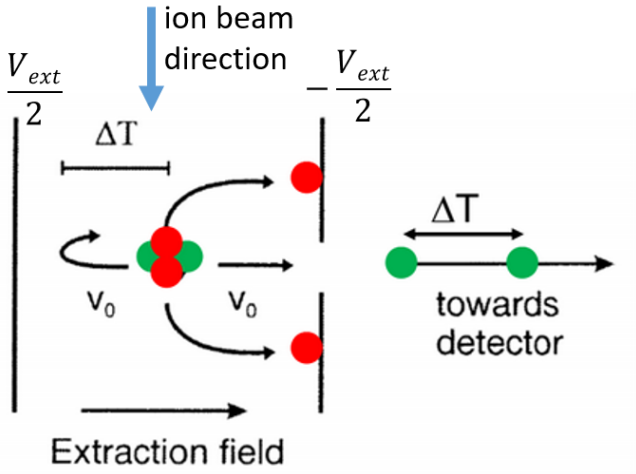

Figure 3.5: Illustration of time-of-flight, showing time difference between forward and backward emitted protons.

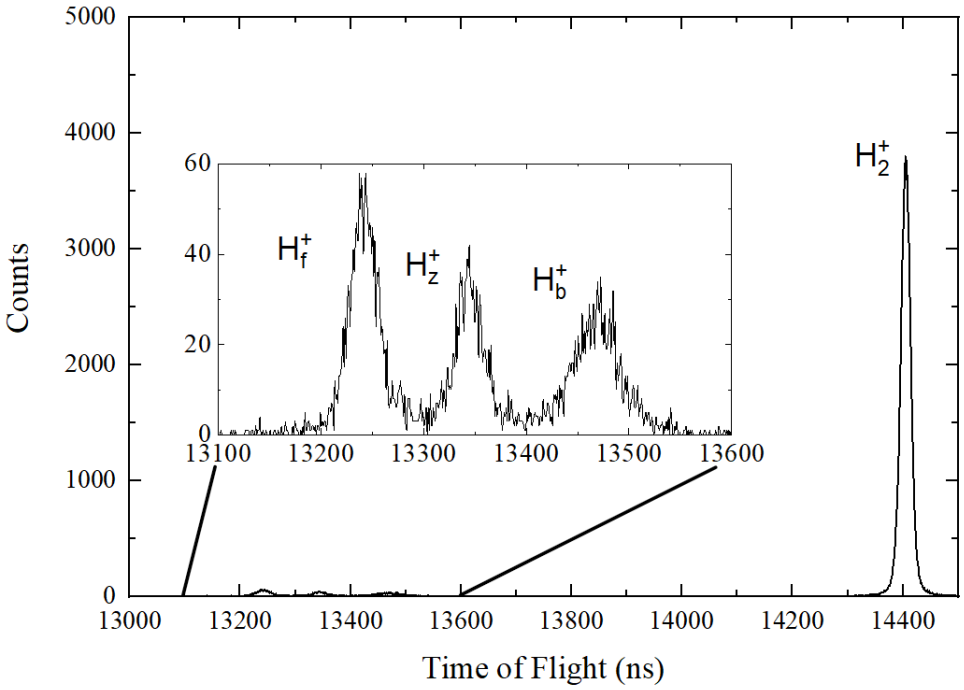

Figure 3.6: Sample time-of-flight spectrum, showing four distinct peaks.

For measurements that did not need a full time-of-flight spectrum (described in 4.1 and 4.3), the rate of charge exchange products striking the MCP was needed. The amplified output of the MCP was plugged into a Tennelec 526 ratemeter, which lets the operator determine the instantaneous count-trate. The Tennelec ratemeter allows for count rate to be measured swiftly, so that effects from beam instability throughout a measurement can be minimized.

4 Results

4.1 Maximizing Target Intensity

The first experiment was conducted using the extraction system from the TOF setup. By fixing two of the three axes, a scan along the free axis can show the position required for maximum intensity. For a symmetrical target profile, the peak along one axis remains in the same position, regardless of what values the other two axes are fixed at.

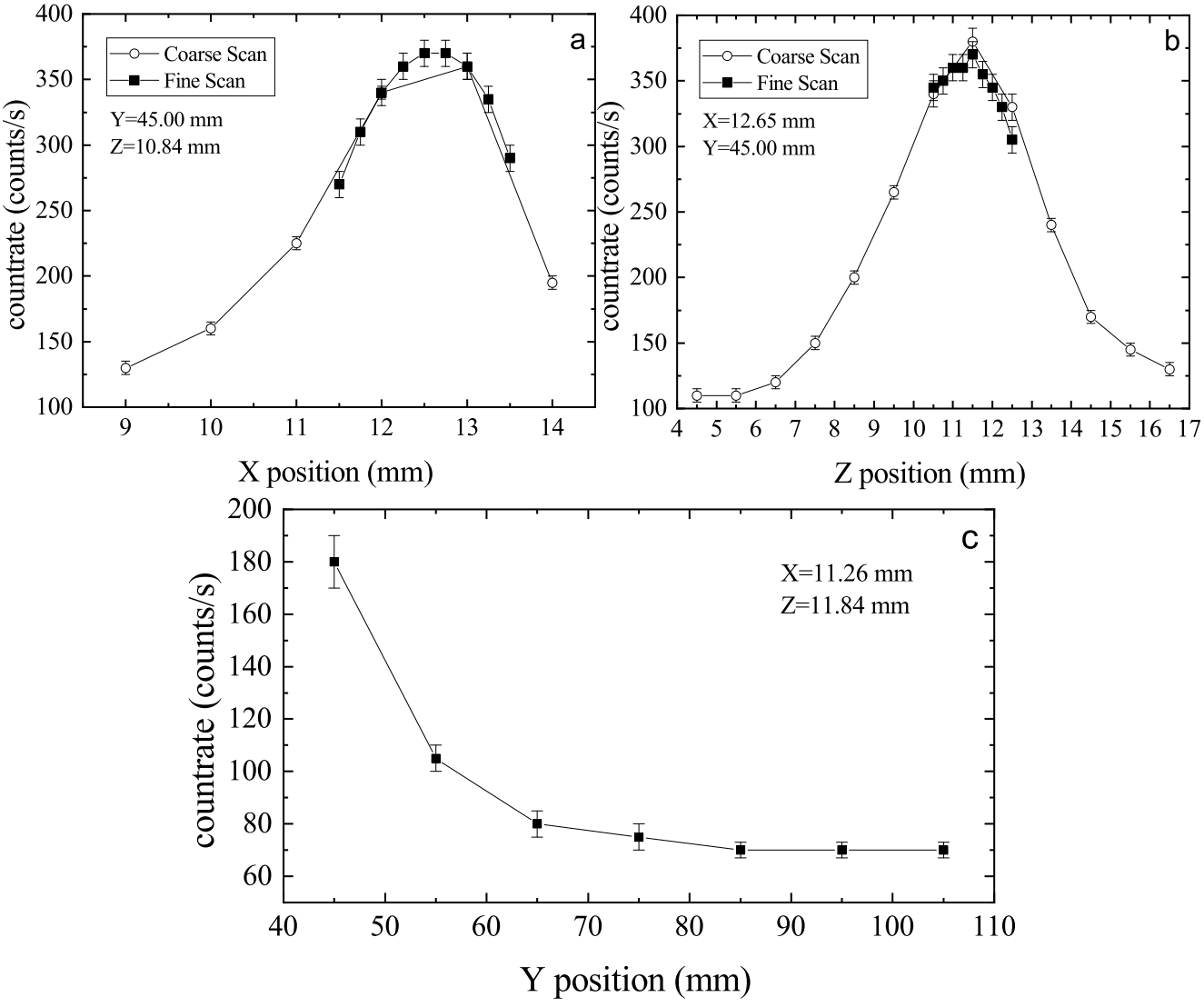

Figure 4.1: Countrate vs. position for a 60 keV O^{6+} beam with an H_2 gas target at 5% flow
a) X scan **b)** Z scan **c)** Y scan

Figure 4.1 shows the results of these position scans. The error in the countrate is discussed in section 5.1. Inspection of the peaks visible in 4.1.a and 4.1.b showed that the optimal position for maximum countrate in the X and Z direction is 12.65 and 11.50 mm respectively. In the Y direction, it was found that the closer one is to the beam, the higher the countrate is. However, the ion beam's exact

position may vary depending on the beam settings. For this reason, one must take care to ensure that the capillary is not in the beam path.

Using the Faraday cup at the end of CHEOPS, the current on the cup (which functions as a measure of the ion beam intensity) was measured as the capillary was moved in the Y direction. Figure 4.2 shows that the Faraday cup current ceases increasing at Y = 43 mm. Based on this, the capillary is assumed to be fully out of the beam at this height.

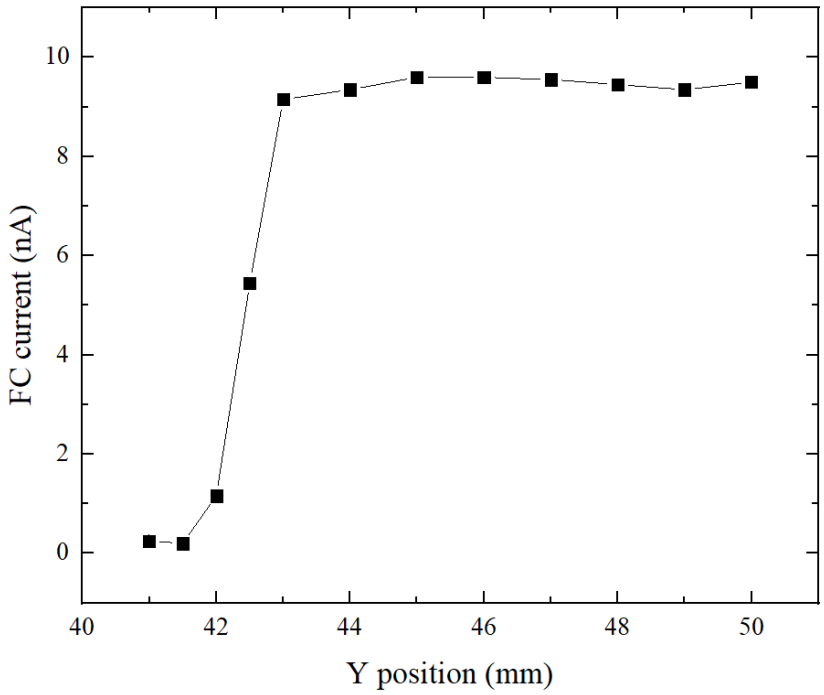

Figure 4.2: Faraday cup current vs. capillary Y position.

4.2 Time-of-Flight: Peak Area Ratios

In this experiment, the position of the capillary was varied along the Y axis, and each time a time-of-flight spectrum was recorded. Using OriginPro's multi-peak fitting algorithm, the area under each peak (corresponding to the number of particles of the peak's species) was determined. Figure 4.3 shows the same sample spectrum shown in Figure 3.6, with fitted peaks and labeled peak areas.

The zero-energy proton peak is largely unaffected (with respect to the other peaks) by the position of the capillary, as any zero energy protons in line with the TOF diaphragm should be transmitted. Figure 4.4 shows how the ratio of measured forward/backward emitted protons to zero-energy protons changes as the capillary's position is moved in the positive Y direction. A decline is seen in the relative number of forward emitted protons as the capillary is increased, whereas the opposite is seen for the relative number of backward emitted protons.

Figure 4.5 shows the ratio of forward to backward emitted protons as the capillary's Y position changes. It is visible that the peak area ratio stabilizes at higher capillary positions. At Y = 47

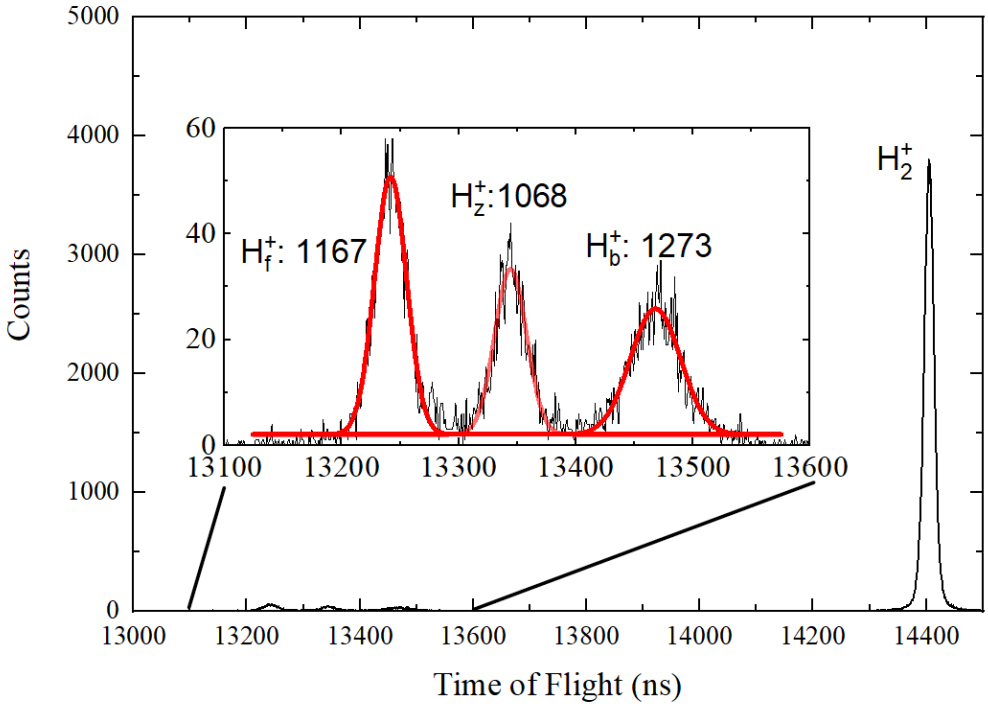

Figure 4.3: Example of OriginPro's multi-peak fitting.

mm, there is already a factor 5 difference in the peak area ratios, compared to Y = 43 mm. However, it was determined that a capillary height of Y = 50 mm is ideal, as the peak area ratio has stabilized and the capillary is physically not in the path of the charge exchange products with respect to the TOF diaphragm. It was hypothesized that the metal capillary may be interfering with the electric field between the charged extraction plates. It is likely that both the capillary-field and the capillary-proton interactions are contributing to the peak area ratio difference seen in Figure 4.5. It is not possible however, to determine to what degree each of these interactions affect the peak area ratios individually. Nevertheless, at Y = 50 mm, the capillary is safely out of the way of the beam and the extraction plates.

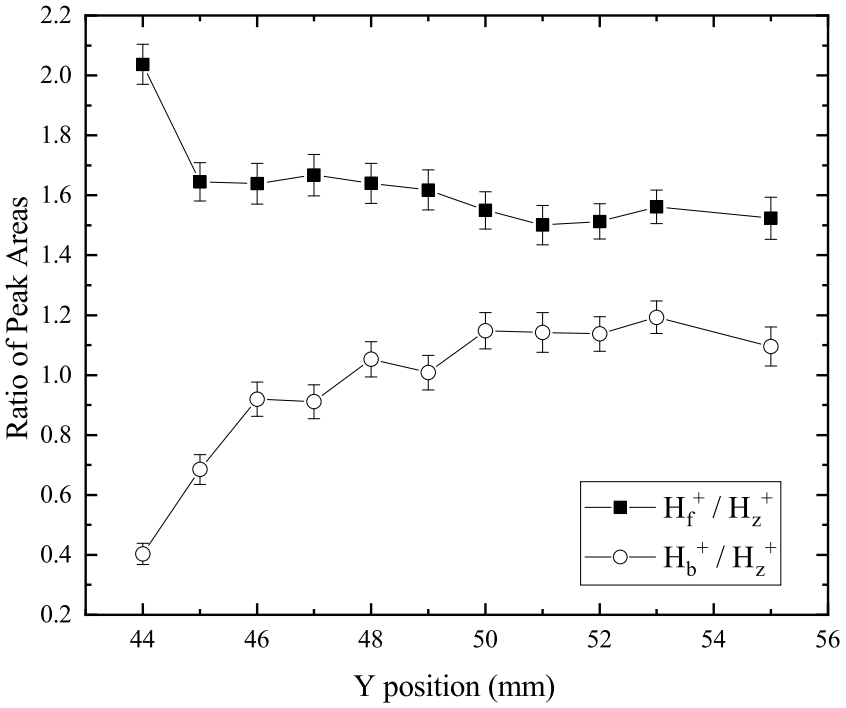

Figure 4.4: Ratio of proton peak areas vs. capillary Y position.

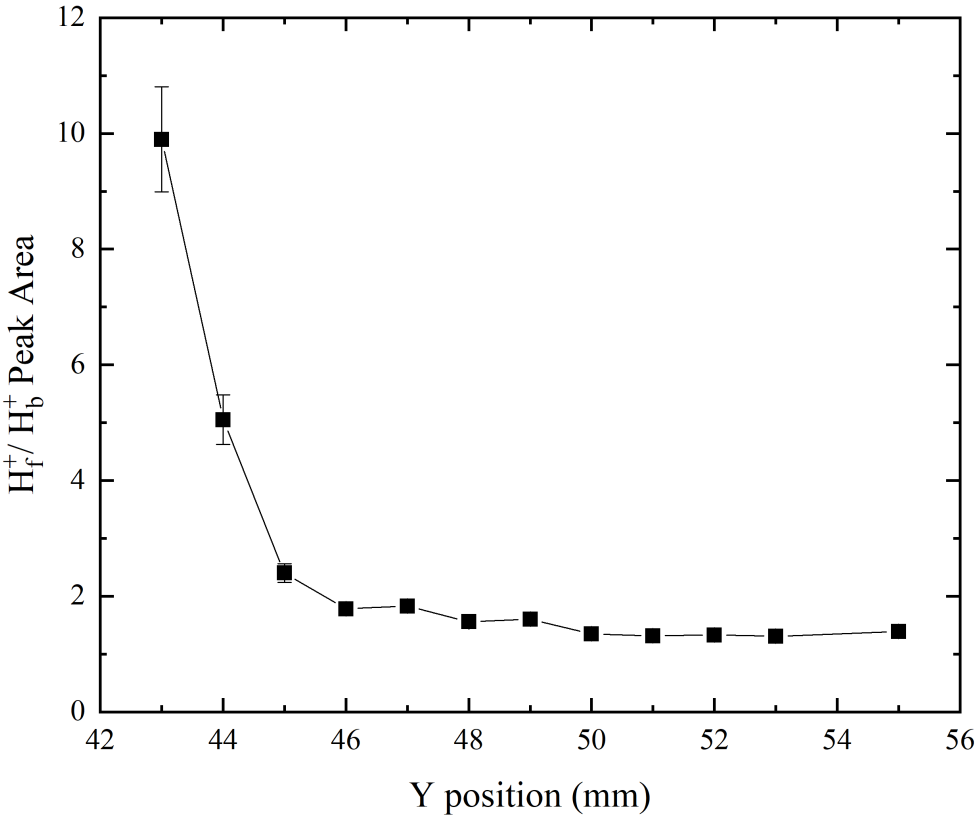

Figure 4.5: Ratio of forward emitted protons to backward emitted protons vs. capillary Y position.

4.3 Target Profile

Lastly, an attempt was made to determine the profile of the H_2 target. Using the ion beam as a probe, the profile characteristics in a selected X-Z plane can be determined. Paired with the assumption that the target profile is symmetrical and Gaussian in shape, the profile of the target can theoretically be determined knowing only the standard deviation of the intensity in one X-Z plane. The mathematical derivation for this can be found in Appendix A.

Once again using the Tennelec 526 ratemeter, the capillary is moved in the X-direction with a fixed Y and Z position. By recording the countrate at set positions in the X-direction, a Gaussian curve begins to form. Over five different target-flow rate combinations, the peak intensity/countrate was determined to be at X = 12.7 ± 0.2 mm, which is well in agreement with the results found in section 4.1.

OriginPro's Single Peak Fitting algorithm was used to determine the full width at half maximum (FWHM) of the Gaussian peaks found from each X-scan. Then by measuring the intensity as a function of Y position, the FWHM at beam-level can be extrapolated to each step in Y. Since this is proportional to the standard deviation (FWHM $= 2\sqrt{2\ln 2}\sigma \approx 2.355\sigma$) the same derivation in Appendix A can be applied to extrapolate the target intensity FWHM for different Y positions of the capillary. This treatment was applied to two different target species: molecular hydrogen (H_2) and molecular deuterium (D_2). The deuterium target was tested at 2, 7, and 20 percent flows, while the hydrogen target was only tested at 2 and 7 percent flows due to time constraints. The results of these measurements can be seen in Figure 4.6. It was noted that the gas pressure in the reservoir was in the order of 1 mbar for 2 and 7 percent flows. This puts us in the transitional flow regime, following equation 1.

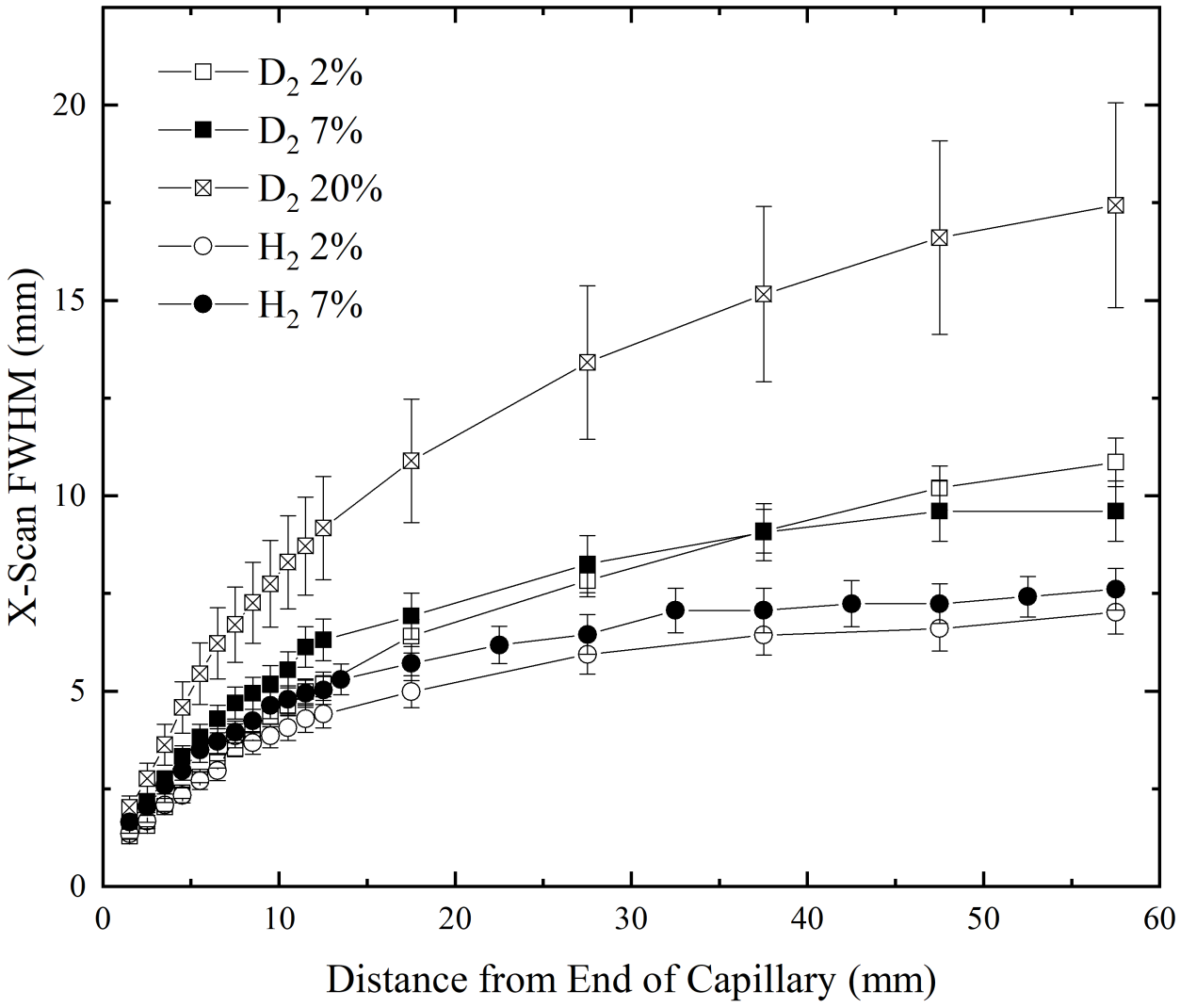

Figure 4.6: Extrapolated X-Scan FWHM vs distance from end of capillary for various targets.

5 Discussion

5.1 Measurement Uncertainty

Measurements in sections 4.1 and 4.3 are subject to reading error from the analog ratemeter. The ratemeter has three scales on the same dial, ranging from 0-2.5, 0-5, and 0-10. Combined with the multiplier dial, which multiplies these scales by factors of 10, the operator can select a setting that allows for the smallest reading error possible. As the countrate measured by the MCP is not constant in time, the ratemeter needle tends to move around erratically. The ratemeter has a dial labeled "% St. Dev." that acts in the same way as a variable time integrator, letting the operator select a value to minimize the signal fluctuation. Figure 4.2 appears not to have error bars because the error in the current is so small it is not visible.

The error visible in the graphs of section 4.2 is purely statistical. The error is derived from the multi-peak fit used to determined the area under each charge exchange product peak. Since these peaks are fit to a histogram, it would be possible to integrate over the bins (which are 1ns in width) directly. However, some peaks overlap slightly, making the error too high with this method. For consistency, all TOF measurements had peaks fit to the histogram. The resulting statistical error is not large enough to obscure the results.

Section 4.3 has errors that are a combination of the error from the Tennelec ratemeter and statistical error. Appendix B shows the derivation for the error visible in Figure 4.6.

5.2 Target Profile

Figure 4.6 may seem to give a clear picture of the target profile, but it is important to understand that FWHM on the vertical axis is not the FWHM in the X dimension, but it is the FWHM of the countrate measured as the capillary is moved along the X direction. It is not possible to probe a point in the CHEOPS chamber, as the only tool available as a probe is the ion beam itself. The ion beam is of finite width, meaning that in the X-Z plane, there is an area in which the target molecules collide with the ions from the beam. The diaphragm to the TOF chamber is 5 mm in diameter, and constrains the area in which charge exchange products can be detected by the MCP.

Figure 5.1 shows a diagram of the "collision area" with respect to the target and the TOF diaphragm. It is important to note that collisions can also occur outside of the collision area, but they will not be detected by the MCP. Including the Y dimension as well, the collision area becomes a 3D volume. While the volume remains the same as the capillary is moved along the X direction, the density of target molecules in the collision volume can change depending on the beam's position with respect to the target. The ratemeter is measuring this target molecule density in the detectable collision volume. Especially close to the center of the target, the detectable collision region includes a large spread of angles from the capillary.This means that the peaks generated from an X-scan may be more flat than those taken by a point probe along the X axis, potentially altering the FWHM. The intensity of the ion beam may also be affected by the density of target molecules in front of the detectable collision area, though it is not possible to quantify this effect without a sufficient theoretical understanding of the target profile.

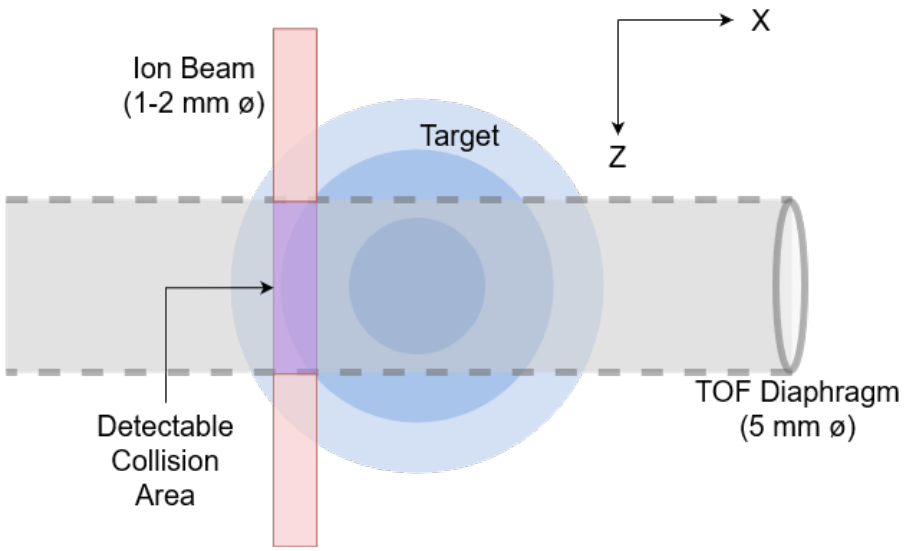

Figure 5.1: Diagram of the X-Z plane, highlighting the detectable collision area.

It is also important to note that the profile shown in Figure 4.6 is based on the assumption that the target is a 3D Gaussian shape. Realistically, the gas effuses from the capillary in a triangular shape from the orifice, though the intensity tends to show a curved peak [5]. Note how in the figure, higher flows lead to wider profiles, for both D_2 and H_2. Further from the capillary, the 7% flow of deuterium appears to be narrower than the 2% flow profile. This unexpected trend is likely to be the result of a degrading ion beam during the Y-scan. Over several days in the lab, it was found that the beam tends to become weaker over time due to magnets heating up or drifting, or instability in the ECRIS plasma. A weaker beam results in a lower measured countrate, meaning that the extrapolated FWHM will also be lower.

5.3 Theoretical Description

There are many difficulties in determining the true shape of the target theoretically. To start, there is an apparent lack of theory predicting the flow out of a capillary in the transition regime. The theory in section 2.3 holds only for molecule-wall interaction in the channel, when the mean free path is much longer than the length of the capillary. Scoles et al. suggest that a theoretical description of flow intensity for this transitional flow regime is too complex [5].

Attempts were made to match the results of section 4.3 to the theory presented in [5]. However, even after trying to adapt the theoretical intensity distribution to the geometry of the setup (using the collision area described above), theoretical predictions were not close to a good fit for the experimental observations. An adjustment can be made to the theory, however. One can assume that the top part of the capillary creates a resistance in the flow, until the mean free path of the particles is suitable for the transparent mode of operation. This decreases the effective length, thereby increasing the effective β. Further work needs to be done in determining the range of validity for this effective β, and whether this approximation holds for higher flow rates from the capillary as well.

5.4 Next Steps

At the end of June 2021, a model was developed to fit the theory from Scoles et al. to the experimental data, that included the effects of the setup's geometry. The results from this model fit the theory more closely than the model described in section 2.3, but not perfectly. While this work is beyond the scope of this thesis, it important to include that the findings from this model show that fitting a Lorentzian peak to the X and Z scans may fit theory more closely than a Gaussian peak. This has a large impact on the predicted background intensity, which is key in determining the FWHM of the scan or target as a whole.

Further comparison between hydrogen and deuterium targets has shown that deuterium has an effective β that is approximately a factor $\sqrt{2}$ times greater than the β of the same percentage hydrogen flow. Predictably, this is due to the mass-velocity relationship of the particles, and the set volumetric flow rate allowed by the flow controller. It is yet to be determined if this relationship holds for higher flow rates.

Further work should be dedicated to determining the range of validity of the effective β approximation described earlier. For now, only low flows have been tested, but the agreement between theory and practice for higher (as in closer to 5 ml/min) flows is yet to be determined.

To make a more accurate theoretical description possible, a multi-capillary array could be used to get a target intensity that is strong enough to run experiments with a low noise level [8]. This array could be used at a low driving pressure, putting the Knudsen numbers in the range that is necessary for free molecular flow. The benefit of such an array would be making a theoretical description of the target possible, but the drawbacks in financing, installation time, and re-calibration time likely outweigh the benefit.

6 Conclusion

Over the month of May 2021, several experiments were conducted to test the operation of the newly installed movable capillary. By fixing two axes and moving the capillary along the free axis, the settings for maximum intensity were found to be X= 12.65, Z= 11.50. For maximum target intensity at the beam, the capillary would ideally be as close as possible to the beam itself, near Y = 43 mm. However, as seen in section 4.2, the capillary is physically blocking some backward emitted protons from entering the time-of-flight chamber. In order to ensure that the metal capillary is not impacting the time-of-flight experiment, it was found that a height of Y = 50 mm is ideal. The effects of the capillary in the electric field have not been measured, but could possibly be simulated in a program such as SIMION.

The profile of the target could be crudely determined via mathematical extrapolation of the FWHM, but due to the geometry of the setup and only having the beam as a probe, the exact dimensions and intensities at specific points could not be determined. Since the pressures in the source region are in the order of 1 mbar, the flow regime is defined as transitional, making a quantitative description of the target difficult, and a theoretical model speculative at best. It would be prudent to conduct an experiment to determine the Knudsen numbers (and therefore the flow regime) more accurately, by measuring the driving pressure more accurately. A theoretical model could be made if the capillary were replaced with a multi-capillary array, though this is impractical.

Beam instability, reading error, and fit error were the main sources of error in these experiments, despite being accounted for as much as possible. Despite the target shape being only loosely known, the setup is now operational and time-of-flight experiments can be run without issue now that optimal settings for intensity have been found.

Bibliography

[1] P. van Gerven, "EUV-emitting tin plasma still harbors surprises." https://bits-chips.nl/artikel/euv-emitting-tin-plasma-still-harbors-surprises/, Techwatch BV. Accessed: 14-06-2021.

[2] P. Atkins and J. De Paula, *Atkins' Physical Chemistry 8th edition*. Oxford Press, 2006.

[3] PfeifferVacuum, "1.2.6 types of flow." https://www.pfeiffer-vacuum.com/en/know-how/introduction-to-vacuum-technology/fundamentals/types-of-flow/ Accessed: 11-06-2021.

[4] F. Rugamas, D. Roundy, G. Mikaelian, G. Vitug, M. Rudner, J. Shih, D. Smith, J. Segura, and M. Khakoo, "Angular profiles of molecular beams from effusive tube sources: I. experiment," *Measurement Science and Technology*, vol. 11, no. 12, p. 1750, 2000.

[5] G. Scoles, D. Miller, W. Gentry, H. Pauly, D. Bassi, U.Hefter, K. Bergman, M. Zen, J. Reuss, C. Meijdenberg, D. Abuerbach, M. Kappes, S. Leutwyler, U. Valbusa, U. Buck, Y. Lee, P. Dagdigian, S. Stolte, R. Düren, and S. Iannotta, *Atomic and Molecular Beam Methods: Vol. 1*. 1998.

[6] Z. Juhász, *Charge exchange processes that make comets radiate*. PhD thesis, University of Groningen, 2004.

[7] E. P. Gilson and J. Fajans, "Quadrupole-induced resonant-particle transport in a pure electron plasma," *Physical review letters*, vol. 90, no. 1, p. 015001, 2003.

[8] S. Adamson, C. O'Carroll, and J. McGilp, "The angular distribution of thermal molecular beams formed by single capillaries in the molecular flow regime," *Vacuum*, vol. 38, no. 6, pp. 463–467, 1988.

[9] R. Klein-Douwel, *Physics Laboratory 1: Data and error analysis*. University of Groningen, 2018.

Appendix

A Target Shape Characterization

Assuming the target is Gaussian in shape:

$$G(x,y,z) = \frac{A}{\sqrt{2\pi}\cdot\sigma(y)}\exp\frac{-(x^2+z^2)}{2[\sigma(y)]^2}$$

At $y = y_0$, $\sigma(y) = \sigma(y_0) = \sigma_0$. Positions x and z are centered with respect to the Gaussian shape of the target at $x = 0$ and $z = 0$.

$$G(0,y,0) = \frac{A}{\sqrt{2\pi}\cdot\sigma(y)} \equiv h(y)$$

$$\implies h(y_0) = \frac{A}{\sqrt{2\pi}\cdot\sigma_0}$$

$$\frac{h(y)}{h(y_0)} = \frac{\frac{A}{\sqrt{2\pi}\cdot\sigma(y)}}{\frac{A}{\sqrt{2\pi}\cdot\sigma_0}} = \frac{\sigma_0}{\sigma(y)}$$

$$\implies \sigma(y) = \sigma_0\cdot\frac{h(y)}{h(y_0)}$$

B Error Propagation

The FWHM is extrapolated using the following formula:

$$\text{FWHM} = \text{FWHM}_{Y=50}\cdot\frac{I_{Y=50}}{I}$$

Where I is the intensity (countrate). The values of $\text{FWHM}_{Y=50}$ are determined using OriginPro's peak fitting algorithm. Each of the three terms has an error associated with it. For I, the error comes from the reading error of the Tennelec 526 ratemeter, but for $\text{FWHM}_{Y=50}$, the error is determined by the fit from OriginPro.

Using standard error propagation techniques described in [9], the error, seen in the error bars of Figure 4.6, can be calculated using the formula:

$$\Delta\text{FWHM} = \text{FWHM}\cdot\sqrt{\left(\frac{\Delta\text{FWHM}_{Y=50}}{\text{FWHM}_{Y=50}}\right)^2 + \left(\frac{\Delta I_{Y=50}}{I_{Y=50}}\right)^2 + \left(\frac{\Delta I}{I}\right)^2}$$